Géotechnique **00**, 1–15 [http://dx.doi.org/10.1680/geot.XX.XXXXX]

Variability of the stress field on intermediate length scales during the triaxial compression of granular materials

IGNACIO GONZALEZ TEJADA*, MARCOS ARROYO†‡, MATTEO CIANTIA§

Defining a continuum stress field in a granular medium involves an approximation, as the underlying contact force network between particles is inhomogeneous and random. The continuum approximation introduces some baseline noise or variability in stress, which becomes more significant as the length scale of interest approaches the typical size of the grains. In this study we evaluate how the stress variability resulting from the homogenization of intergranular forces changes as the homogenization scale is increased. This is done by obtaining the probability distribution function of stresses from a large number of repeated discrete element method based simulations of the triaxial compression of granular samples. The numerical experiments share sample dimensions, generation protocols and imposed stresses, but involve randomly generated sets of granular packings made of different numbers of particles. The results from this study are used to propose and develop a consistent general framework to rigorously describe mesoscale stress fields and hence fill the gap between existing micro and macro mechanical approaches. A backbone curve is obtained expressing the change in stress variability as the mesoscale is traversed. The results deduced from the backbone curve are in good agreement with those of independent numerical and physical experiments on granular soils.

KEYWORDS: Statistical Analysis; Discrete Element Modelling; Granular materials; Stress analysis; Micro-nano geomaterials

INTRODUCTION

Grounding continuum descriptions of granular soil behaviour on particle scale micromechanics adds theoretical consistency to soil mechanics but is also advantageous form a practical viewpoint. For instance, it facilitates material model calibration, as it is frequently simpler to gather particle-scale information than specimen-scale information. Much work in this respect has been directed to establish the micromechanical basis of continuum level constitutive descriptions, for instance in models that incorporate fabric variables Wang *et al.* (2021) or grain-derived properties Kikumoto *et al.* (2010). On the other hand, less attention has been paid to fundamental questions, for instance those underlying the assumption of a continuum stress field. Stress fields are meant to be univocally defined at any point in the continuum and to vary smoothly in space. However, these stress fields emerge from granular interactions that are very far from those requirements. Our focus here is on how the evident heterogeneity and randomness of granular material force interactions at the grain scale propagates and attenuates as we approach the continuum scale.

Photoelastic and numerical experiments Drescher & de Josselin de Jong (1972); Radjai *et al.* (1996) unveiled that external loads on granular packings are supported by a stochastic system of interparticle forces. The statistics and topology of those forces (Fig. 1a) has attracted considerable attention from the scientific community (*e.g.* h. Liu *et al.* (1995); Jaeger & Nagel (1996); Coppersmith *et al.* (1996); Radjai *et al.* (1996); Mueth *et al.* (1998); Radjai *et al.* (1999); Majmudar & Behringer (2005); Peters *et al.* (2005); Radjai (2015)). Results from these studies highlight two important aspects of the problem:

1. Inhomogeneity: Forces may considerably change from one particle to another, even for direct neighbours. The system of interparticle forces is organized into weak and strong forces networks Radjai *et al.* (1996).
2. Randomness: There is a vast number of different ways to keep the same granular system in static equilibrium under the same imposed boundary conditions. As a result, the values of the forces acting on any particle do not depend on its position with respect to the macroscopic boundary value problem but also on the specific realization of the experiment.

The statistical distribution of forces is directly relevant for some applications, for instance when studying the crushing of particles Frossard *et al.* (2012); Alonso *et al.* (2012); Ciantia *et al.* (2015, 2016b,a); Wang *et al.* (2021); Ciantia *et al.* (2019). However, stresses are more useful for most geotechnical engineering applications. Equivalent stresses are obtained from intergranular contact forces by means of homogenization techniques. For instance, the Love-Weber stress is widely applied to obtain equivalent stresses for particles in static arrangements Bagi (1996); Nicot *et al.* (2013) (Fig. 1b):

$$\langle \sigma_{ij} \rangle^m = \frac{1}{V^m} \int \sigma_{ij}^m dV^m = \frac{1}{V^m} \sum_n r_i^{mn} F_j^{mn}, \quad (1)$$

where V^m is the volume of the Voronoi cell associated to particle m, F_j^{mn} is the j-component of the interaction force between particles m and n and r_i^{mn} is the i-component of the branch vector (*i.e.* the vector connecting the centers of gravity of particles m and n). Although interparticle forces can be transformed into equivalent stresses, this field varies from one particle to another. To establish a continuum stress field (extending over the solid parts and the voids), Voronoi tessellations may be used to assign a volume to each particle, creating a pattern of cells that leaves no gaps (*e.g.* Chareyre *et al.* (2012)). The same Love-Weber homogenization technique can then be applied to obtain equivalent (average) stresses for each Voronoi cell (Fig. 1c). However, by itself, tessellation is not enough to erase the inhomogeneity and randomness found in the network of interparticle forces. The equivalent stress field is stochastic and still non-smooth on length scales involving a

Manuscript received...
* Universidad Politécnica de Madrid, Madrid, Spain, † Centre Internacional de Mètodes Numèrics en Enginyeria (CIMNE), Barcelona, Spain, ‡ Universitat Politècnica de Catalunya (UPC-BarcelonaTECH), Barcelona, Spain § Dundee University

few particles. Indeed, the variability of microscale stresses in Voronoi granular cells may be described by statistical distributions Tejada (2020).

Homogenization can also be applied at larger scales, obtaining stress in control regions defined to include multiple Voronoi particle cells (Fig. 1d)). By the law of large numbers, and independently of the statistical distribution of microscale stress (provided that it has a finite variance), the higher is the number of particles in those regions, the lower is the variability of the average stress. In fact, if microscale stresses are considered as independent random variables, the normalized sum tends toward a normal distribution even if the original variables themselves are not normally distributed (central limit theorem). This reasoning allows a meaningful definition of macroscale as the scale reached when the variability of the average stress is negligible. At the macroscale the stress field is well behaved and continuum mechanics is of direct application.

A challenging problem arises at intermediate scales, where the truly discrete nature of the soils cannot be ignored. These situations occur when the length scale of interest is larger than the typical size of the grains but not large enough. The intermediate scale is herein referred to as the *mesoscale*, in opposition to the *microscale*, which would refer to length scales that are close to the typical size of the grains, and the *macroscale*, which would refer to a scale on which the body behaves as a continuum for all practical purposes.

Mesoscale stresses can be relevant in several circumstances that frequently arise in soil mechanics:

- In laboratory testing with specimens made of particles of size comparable to the device dimensions (*e.g.* testing of railway ballast, gravels, etc.)
- In field techniques where stress is measured, be that through passive instruments such as diaphragm-type stress cells Weiler & Kulhawy (1982) or through active instruments, pushed into the ground, such as the Cone Penetration Test.
- In numerical modeling with discrete models: as these models use to be computationally expensive, efficient procedures to simulate large-scale soil volumes are needed Mcdowell *et al.* (2012); Ciantia *et al.* (2018). In order to establish the size of representative volumes, it is important to understand how close to particle size the characteristic dimensions of the simulated problem can be.

In all these cases, where the experiment or simulation is forced to operate within the mesoscale, the distinct nature of particles must be considered. In particular, it would be useful to evaluate precisely the contribution of the stochastic variation of the stress field inherent to the mesoscale to the overall observed variability of an experimental or numerical output.

Mesoscale stress is also relevant in a variety of engineering design situations, where some length scale of the problem is similar to the typical particle size. This is the case in a variety of soil-structure interaction problems, for instance that between railway ballast and railroad ties Alabbasi & Hussein (2021), but also to address soil-fluid interaction, in problems like overtopping erosion of rockfill dams Larese *et al.* (2015), transport of particles through granular assemblies during suffusion processes Tejada *et al.* (2016), filters Shire & O'Sullivan (2016); Taylor *et al.* (2019), etc.

Finally, understanding how stress uncertainty varies with scale is also directly relevant for multiscale constitutive approaches transitions between micro- and macro- mechanics. For example, for data-driven frameworks that predict macroscopic macroscopic properties Tejada & Antolin (2021).

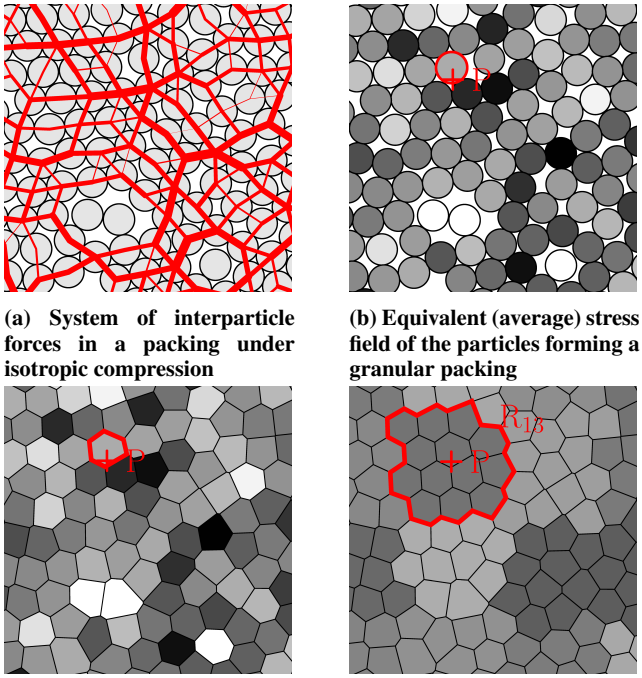

(a) System of interparticle forces in a packing under isotropic compression

(b) Equivalent (average) stress field of the particles forming a granular packing

(c) Equivalent (average) stress field on the microscale (Voronoi regions associated to particles)

(d) Equivalent (average) stress field on the mesoscale (control regions including several particles)

Fig. 1. Simplified schematic of interparticle normal forces and equivalent stress field at different length scales in a 2D granular packing under isotropic compression

The purpose of this work is to quantify stress variability at the mesoscale in granular soils. To this end we study an idealized granular system subject to drained triaxial compression. Results from a large number of 2D and 3D DEM simulations (more than 4500) at different scales are analysed statistically so as to obtain probability distribution functions of forces and stresses in the mesoscale transition. In what follows we first recall some results relating to microscale stress statistics that lay the ground for the current analyses. We then describe the methodology employed for the numerical experiments, present the results obtained and discuss their implications in the light of some previously available experimental and numerical data.

STATISTICS OF MICROSCALE STRESSES

Statistical mechanics Balescu (1975); Pathria & Beale (1996) is particularly useful in this context, as it provides a rational way of exploring all possible solutions to a problem and to anticipate the most likely statistical distribution of some variables compatible with the problem constraints. Important contributions to the statistical mechanics of athermal granular systems are due to Edwards & Oakeshott (1989); Edwards *et al.* (2003); Edwards (2005); Henkes *et al.* (2007); Henkes & Chakraborty (2009); Tejada (2014) amongst others. Some of these approaches Henkes *et al.* (2007); Henkes & Chakraborty (2009); Tejada (2014) were based on the extensive stress concept. Extensive stress is measured in energy units and defined as the product of the volumetric average stress field within a region and the volume of that region. According to Equation 1, extensive stress can be obtained directly as

$$\Sigma_{ij}^{m} = \langle \sigma_{ij} \rangle^{m} V^{m} = \sum_{n} r_{i}^{mn} F_{j}^{mn}. \qquad (2)$$

Tejada (2020) used extensive stress to develop a stochastic model for the average stresses in Voronoi tessellations of granular media. This model was built on the following hypotheses:

(i) The stress field is uniform within a Voronoi cell.
(ii) There is no spatial correlation between the extensive stress of several control regions and there is no correlation between different realizations of the same experiment.
(iii) The stress field obtained as a solution to the corresponding boundary value problem treating the discrete medium as a continuum is referred to as the *macroscopic stress field*. The values of normal and shear components of the stress tensor in any cell, when expressed in the principal directions of the macroscopic stress field, are uncorrelated.
(iv) The extensive stress tensor of a cell may take any allowed value provided that, if the experiment is repeated many times, the values of its components follow statistical distributions whose mean values match those of the macroscopic stress field. More precisely, in the principal directions,
  iv-a normal components (parallel to principal directions) can take only positive values (tensile interparticle forces do not exist in the interaction model and particles do not break or deform) and their mean values, when all possible solutions are considered, are the principal stresses,
  iv-b shear components can take either positive or negative values provided that the mean value of all compatible solutions is null and that the absolute difference from the mean is limited by interparticle friction, particle shape and size distribution and the magnitude of normal components.

Under such constraints, the normal and shear components of the stress in Voronoi cells were demonstrated to follow exponential and Laplace distributions, respectively Tejada (2020). The work of Tejada (2020) was limited to the microscale and did not explore the mesoscale. In what follows we demonstrate that given a PDF of microscale stresses a generalization of the Tejada & Antolin (2021) approach to the mesoscale is possible.

METHODOLOGY

Overview

To explore stress variability at the mesoscale, idealized granular packings are studied using the discrete element method, DEM Cundall & Strack (1979). Several series of virtual experiments are performed using the same packing arrangement protocol, stress path and stress levels and similar dimensions of the simulation box. Elements are spherical particles whose diameters were distributed within an interval around the mean size ($\pm 2\%$) for quasi monodispersed samples or continuously distributed, in weight, between half and double the mean size (polydispersed samples). In the case of monodispersed packings, three different mean diameters are employed to build simulation sets with significantly different numbers of particles (Table 2). Average stress fields are measured on the microscale (average stress field within a Voronoi cell) and on the mesoscale (with control regions that included, on average, between 1 and 1000 particles). After a massive repetition of triaxial experiments (more than 4500 in total), sets of statistical samples are gathered to analyse the PDFs of forces and stresses.

Table 1. Parameters used in the numerical experiments

Property		Value
Young's modulus	E	10^4 kPa
Tangential to normal stiffness ratio	$k_\mathrm{s}/k_\mathrm{n}$	0.3 [–]
Interparticle friction angle	ϕ	0.5 rad
Side of the simulation box	l	0.1 m
Isotropic compression stress	p	50.0 ± 0.2 kPa
Maximum principal strain	ε_1	0.02 [–]

Discrete model

There is a long track record of research Thornton (2000); Ng (2004); Sibille *et al.* (2007); Kozicki *et al.* (2014); Salot *et al.* (2009); Zhou *et al.* (2017); Xie *et al.* (2017); Wu *et al.* (2021) demonstrating the capabilities of DEM for the study of granular materials in triaxial compression.

In this work DEM is applied as implemented in the code YADE-DEM Šmilauer *et al.* (2015)*. The elements selected are spherical particles (3D) or circular disks (2D) interacting with each other through frictional-Hookean contact laws. If the overlap is defined as $\delta^{mn} = (R^m + R^n) - \mathbf{r}^{mn} = (R^m + R^n) - |\mathbf{r}^m - \mathbf{r}^n|$, where R^m and R^n are the radii and $\mathbf{r}^m$ $\mathbf{r}^n$ are the position vectors of particles m and n, respectively, then the normal contact force acting on particle m due to its contact with particle n is:

$$\mathbf{F}_\mathrm{n}^{mn} = -k_\mathrm{n}\delta^{mn}, \tag{3}$$

where the contact stiffness is $k_\mathrm{n} = 2ER^mR^n/(R^m + R^n)$ and E is the Young's modulus (Table 1).

Tangential forces are produced in opposition to incremental lateral displacements. Lateral forces are limited, and the threshold is in each case proportional to the value of the associated normal force. The ratio is given by the friction coefficient (defined as the tangent of the inter-particle friction angle, ϕ).

$$\mathbf{F}_\mathrm{s}^{mn} = -\min\left(k_\mathrm{s}u^{mn}, \tan\phi|\mathbf{F}_\mathrm{n}^{mn}|\right)\mathbf{u}^{mn}/|\mathbf{u}^{mn}|, \tag{4}$$

where u^{mn} is the lateral displacement between the two particles previously in contact ($\delta^{mn} \geq 0$) and k_s is the tangential stiffness, taken proportional to k_n. Local numerical damping Cundall (1987) was used to dissipate kinetic energy: Forces that increase the particles' velocities are decreased by adding damping forces by component. The on-step estimate of the velocity, rather than the previous mid-step velocities, was used. Gravity acceleration was not considered. The contact parameter values applied are reported in Table 1; the values were chosen to represent qualitatively granular soil behaviour.

Numerical experiments

Numerical experiments were performed on periodic cells, generally using cubical (3D) cells but also, for comparative purposes, square (2D) cells. Although 3D DEM experiments offer a better analogue for granular soils, 2D experiments are also often employed because of it much reduced computational cost Adesina *et al.* (2022). Stress variability at the micro and mesoscale may differ from one case to the other, since the number of dimensions determines the number of balance constraints on the microscale (*i.e.* the force and moment balance on each particle) as well as the features of the contacts network (*e.g.* PDF of coordination numbers). Four different particle size distributions, PSD, were employed in

*https://yade-dem.org/.

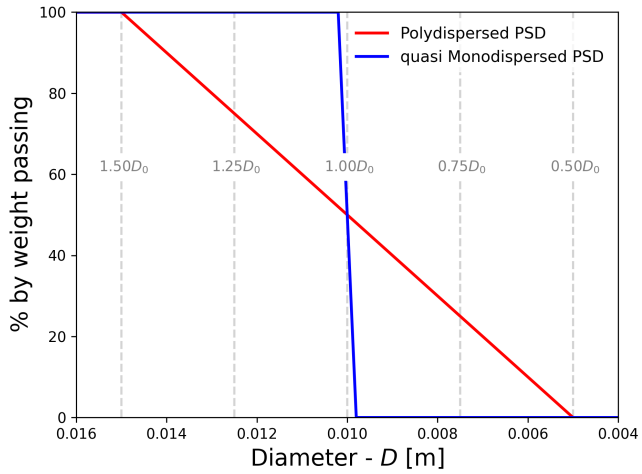

Fig. 2. Particle Size Distribution (Cumulative Distribution Function) of the samples used in the numerical experiments

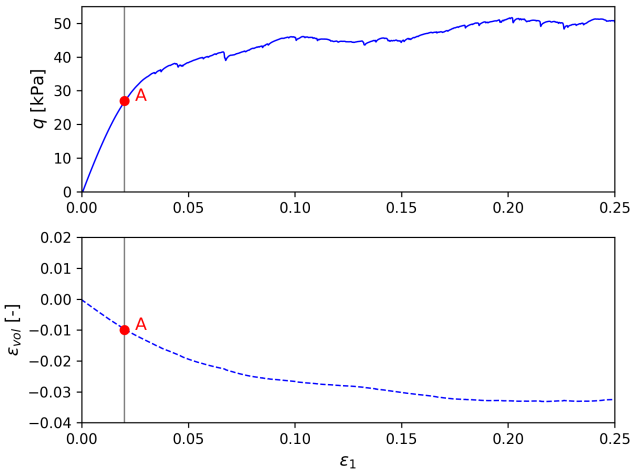

Fig. 3. Simulated behaviour of loose sand as observed in numerical triaxial compression test on a 3dL specimen (3375 particles) run until ($\varepsilon_1 = 0.25$). Points A indicate the strain level at which the statistical analyses take place ($\varepsilon_1 = 0.02$). Top figure: Deviatoric stress $q = 0.5\,(\sigma_1 - \sigma_3)$ *vs.* major principal strain. Bottom figure: Volumetric strain *vs.* major principal stress (compressive)

the 3D cells. Three of them were quasi monodispersed with different mean grain size (D) each of them. The fourth PSD was polydispersed (Fig. 2). The resulting experimental sets are subsequently referred to as large monodispersed (3dL), medium monodispersed (3dM), small monodispersed (3dS) and large polydispersed (3dLpoly). The different diameter sizes produced samples with different numbers of particles (see Table 2).

Each numerical experiment comprised the following steps:

0 *Sample generation* A cubic simulation box with periodic boundary conditions was filled with a random and loose cloud of spherical (or circular in 2D) particles. In the case of quasi-monodispersed samples, the diameters of the particles were uniformly distributed within the interval $D \pm 2\%D$ and the dimensions of the cube were chosen so that after the isotropic compression (step 2 below) its side was always the same (l). In the case of the polydispersed sample, the diameters of 3000 particles were chosen according to the PSD shown in Fig. 2.

1 *Isotropic compression*. The simulation boxes were progressively reduced in size until achieving a target isotropic compression stress p. The maximum strain rate was limited $0.01\ \mathrm{s}^{-1}$.

2 *Deviatoric compression*. A strain ε_1 was imposed in the principal direction 1 while maintaining the lateral stresses constant ($\sigma_2 = \sigma_3 = p$). The maximum strain was stopped at $\varepsilon_1 = 0.02$ in order to maintain the specimen macroscopic responses in a quasi-linear regime (see Fig. 3) with deviatoric stress at about 60% of their failure level (major principal stress σ_1 in the range $76.7 - 78.3$ kPa). During compression, the maximum unbalanced force was always controlled to ensure a quasistatic process.

The numerical experiments were repeated a large number of times for each model (Table 2) in order to gather large statistical samples that make it possible to draw the PDF of the stresses both at the micro and mesoscales. The dispersion of each of these PDFs will depend on the number of particles involved but the high number of repetitions serves to unveil these PDFs with considerable accuracy. Data from each experiment was acquired for postprocessing at the end of the isotropic stage and at the reference deviatoric compression stages. Equivalent stresses were measured on two scales:

- At the microscale (grain level): In every realization we sample cell stress at the Voronoi cells that englobe certain spatially fixed control points. To obtain a large statistical sample, as shown in Fig. 4, 7 control points were employed. Note that, for ease of visualization, Fig. 4 illustrates a 2D scenario although the same concept was employed for the 3D simulations. Of these control points, one (point O) was located at the centre of the cubic specimen, while the remaining 6 points P (4 in 2D) were located halfway between point O and each box side. Point Q (near a box corner) was employed to verify the influence of the sampling point location. The continuum stress field is the same for all these points and the distance between them was enough to make them uncorrelated (Fig. 5). In 2D tests the number of microscale sampling points P was reduced from 6 to 4.
- At the mesoscale (region level): In every realization we computed the stress field average for cubic control regions of varying sizes, named R_N, which are always co-centric with the sample box (Fig. 4). The size of the cubic control regions was adjusted so as to include, when possible, a given average number of particles throughout the experiment series $N = 1, 5, 40, 300, 1000$. For example, the volume of region R_5 was chosen to always include around 5 particles, so its dimensions changed with the typical size of the particles used in the simulation series. It is worth mentioning that if the whole simulation box is used as a control region the average stress will not fluctuate, as this is precisely the scale on which the stress is externally controlled. To avoid sample size effects, we limit the use of the control regions in each series so that the largest control region includes no more than one third of the total particles in the granular packing. On the other hand, the number of particles within each control region changes with each specific realization of a packing and this variability is more significant for the smallest control regions and for polydisperesed samples. For example, R_1 contains 1 particle on average but in some realizations it will be empty and in some cases it will include more than one particle (especially when the sample is polydispersed). As a result, the micromechanical stress

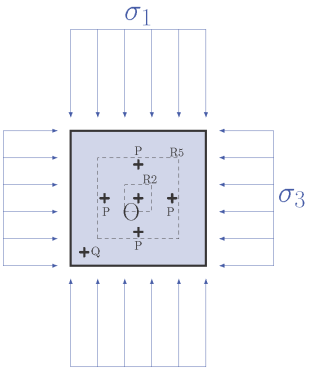

Fig. 4. Schematic 2D version of the virtual samples showing the control points O, P and Q, as well as some control regions (R_2, R_5). Note that most of the simulations performed in this research were 3D

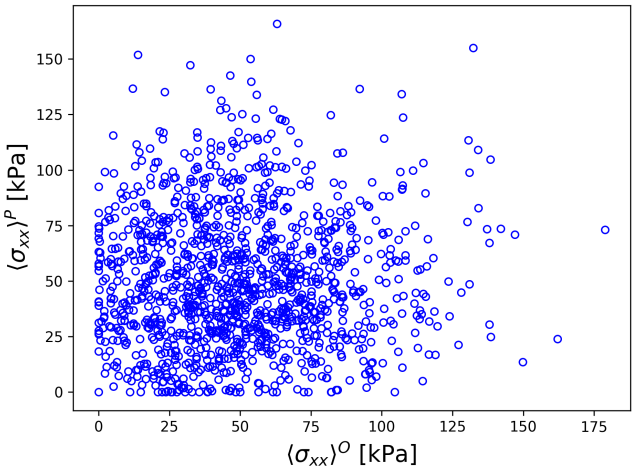

Fig. 5. Correlation between the values of $\langle\sigma_{xx}\rangle$ measured at point O and one of the points P (Fig. 4): Results from the 3dM experiments (1000 particles) after isotropic compression. The Pearson correlation coefficient in this case is $\rho = -0.036$.

(*i.e.* the equivalent stress of the closest particle to a control point) may differ from the stress measured within a control region having 1 particle on average. The former is referred to as stress on the microscale and denoted as $\langle\sigma_{ij}\rangle$ and the latter is referred to as stress on the mesoscale within a region containing one particle on average and denoted as $\langle\langle\sigma_{ij}\rangle\rangle^{R_1}$.

Particles non transmitting loads (rattlers) were not considered for the statistical study of stresses measured on the microscale. On the mesoscale however, its null contribution is taken into account, *i.e.* stress averaging is performed over a region R that may include rattlers.

RESULTS

Force distributions

One of the 3dL experiments (involving 3375 particles) was used to analyze the statistics of interparticle forces. After the isotropic compression stage (step 1), a loose packing (with average porosity of $n \simeq 0.42$ and average mechanical coordination number of $N_c \simeq 5.36$) was examined. The PDF of the interparticle normal forces in this numerical experiment is shown in Fig. 6. This PDF presents a bimodal organization of the force network in well-defined weak and strong networks,

Table 2. Characteristics of the numerical experiments

Feature (1)	Experiment (2)				
Label	2dS	3dS	3dM	3dL	3dLpoly
Dimensions	2	3	3	3	3
No. of particles	324	343	1000	3375	3000
No. of tests	768	1160	1275	1412	985
Diameter ($\times 10^{-2}$ m)	1.06	1.42	1.00	0.67	$0.5 - 1.5$

Table 3. Features of the packings generated during the numerical experiments

Feature (1)	Experiment (2)				
Label	2dS	3dS	3dM	3dL	3dLpoly
Ave. No. of particles					
in region R_1	324	1	1	1	1
in region R_5	5	5	5	5	5
in region R_{40}	43	40	39	41	41
in region R_{90}	89	90	91	91	89
in region R_{300}	N/A	N/A	301	302	301
in region R_{1000}	N/A	N/A	N/A	1015	997
Isotropic compression					
Side, l ($\times 10^{-1}$ m)	1.82	0.97	0.97	0.97	0.56
Porosity (-)	0.18	0.42	0.42	0.42	0.39
Rattlers (%)	0.18	2.1	7.92	9.29	15.8
Isotropic stress (kPa)	5.0	49.5	49.5	49.5	49.5
Deviatoric compression ($\varepsilon_1 = 0.02$)					
Lateral stress (kPa)	5.1	50.0	50.0	50.0	50.0
Vertical stress (kPa)	6.4	76.3	76.7	77.3	81.9

what has been previously observed experimentally Løvoll *et al.* (1999) and numerically Antony (2000). The observed exponential decay of the PDF of strong forces is robust feature of force distribution in granular media, whereas for the network of weak forces, the PDF has been claimed to be sensitive to the packing state resulting from the deformation history Radjai *et al.* (1996); Radjai (2015). For instance Metzger (2004) showed, for packings under isotropic compression, features such as those visible in Fig. 6, *i.e.* a small second peak below the mean force and a PDF of small forces that does not fall to zero.

The normalized magnitude of the strong forces shows the expected exponential decay. The mean normal force in this experiment was $\overline{F_n} = 2.25$ N. Considering that in this simulation the average diameter was $D = 0.067$ m, this mean normal force corresponds to an average overlap of $\overline{\delta} = 6.7 \cdot 10^{-5}$ m (*i.e.*, $\overline{\delta} \sim 0.01D$), which is small enough to ensure that the shapes of the particles are not altered too much.

Microscale stress distributions

Microscale stress $\langle\sigma_{ij}\rangle$ is measured at the level of a Voronoi cell at a given point. Most of the microscale stress distributions are presented in normalized form. Non-normalized forms are included to show the effect of the macroscopic stress conditions when going from isotropic compression to triaxial compression states. Normalization is made using the sample mean and standard deviation. The statistical sample is gathered after $\mathcal{N}$ realizations of each model, see Table 2. The sample mean is

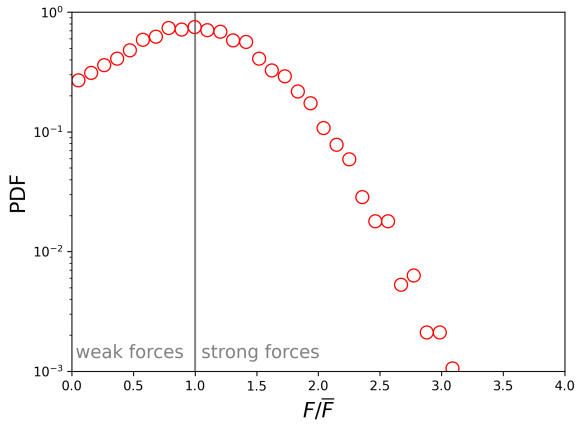

Fig. 6. Normalized PDF of interparticle normal forces obtained from a packing made of 3375 particles subjected to isotropic compression)

defined as

$$\overline{\langle \sigma_{ij} \rangle} = \frac{\sum_{n=1}^{\mathcal{N}} \langle \sigma_{ij} \rangle_n}{\mathcal{N}}, \tag{5}$$

and the sample standard deviation is defined as

$$s_{\mathcal{N}\langle \sigma_{ij} \rangle} = \sqrt{\frac{1}{\mathcal{N}-1} \sum_{n=1}^{\mathcal{N}} \left(\langle \sigma_{ij} \rangle_n - \overline{\langle \sigma_{ij} \rangle} \right)^2}. \tag{6}$$

As expected, the sample mean matches the values given by the macroscopic stress field corrected by the proportion of rattlers, *i.e.*

$$\overline{\langle \sigma_{ij} \rangle} \simeq \mu_{\langle \sigma_{ij} \rangle} = \sigma_{ij} / (1 - r), \tag{7}$$

where σ_{ij} is the corresponding component of the externally imposed macroscopic stress field and r is the proportion of rattlers in the packing. The number of rattlers in the 3D experiments under isotropic stress compression ranged between 2.1% and 15.8%, increasing with sample size and polydispersivity.

The macroscopic stress field determines the statistical distribution of the stress on the microscale, with differences between isotropic and deviatoric stress conditions. This is evidenced by the observed evolution of the non-normalized PDFs of several variables when going from an isotropic compression state, $\sigma_{xx} = \sigma_{yy} = \sigma_{zz} = \sigma_1 = \sigma_3 \simeq 50$ kPa ($p = 50$ kPa, $q = 0$ kPa), to a deviatoric compression state of $\sigma_{xx} = \sigma_{yy} = \sigma_3 = 50$ kPa and $\sigma_{zz} = \sigma_1$ in the range $76.3 - 81.9$ kPa ($p = 50$ kPa, q ranging between 13.1 and 15.9 kPa). Figures 7 and 8 show non-normalized PDFs for the 3dM triaxial experiments series. The application of the deviatoric compression in the vertical direction, z, changes the PDF of vertical and major principal stresses, while those of horizontal (x and y) and minor principal stresses remain unaltered (Figs. 7a and 7b). The deviatoric stress also changes the PDF of the center, $\langle p \rangle$, and radius, $\langle q \rangle$, of the Mohr's circles associated to the equivalent stress field of the Voronoi cells (Fig. 8a), increases the number of cells presenting a failure ratio $\eta = \langle q \rangle / \langle p \rangle$ closer to 1.0 (Fig. 8b) and reorients the direction of major principal stresses (which tends to be more parallel to the vertical direction, Fig. 8c).

Although the isotropic and deviatoric stress conditions considered in this research present differences in the PDFs associated to the stress field on the microscale, these differences may disappear when the PDFs are normalized. The influence

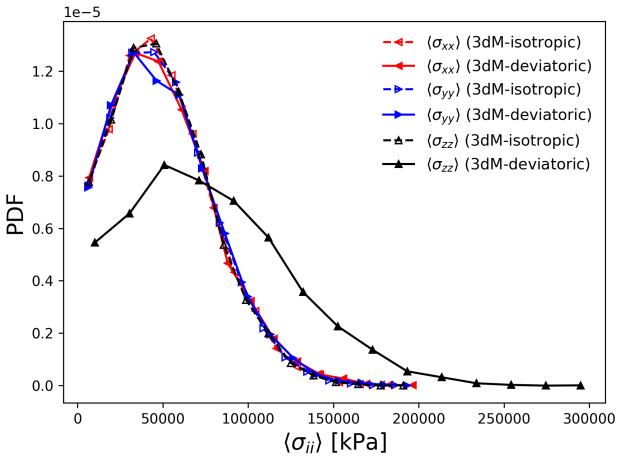

(a) PDFs of normal stresses

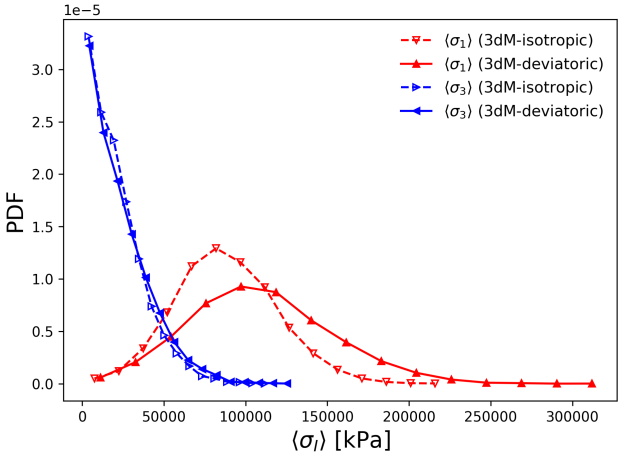

(b) PDFs of major and minor principal stresses)

Fig. 7. Non-normalized PDFs of the stresses on the microscale under isotropic and deviatoric stress conditions

of the sampling point location on the characteristics of the microscale stress distribution was examined by checking the PDF of normalized microscale average normal stress, sampled in realizations of model 3dL at either point O alone or a point Q alone, as well as that obtained when sampling at the 7 pre-established locations (points O and P) (Fig. 9). The distributions obtained when sampling at a single point (either O or Q) are very similar to those obtained when all the sampling points are employed. The differences appear to increase towards the higher end of the distribution, where larger samples are more reliable. Several PDFs of stresses measured on the microscale and expressed in a normalized way are also shown in Fig. 10. These distributions are compared with Gamma distributions, whose probability density functions (PDF) are written as Forbes *et al.* (2011):

$$f_{(k,\theta)} = \frac{x^{k-1} \exp(-x/\theta)}{\theta^k \Gamma_{(k)}} \qquad x \geq 0. \tag{8}$$

k is the shape parameter, θ is the scale parameter and

$$\Gamma_{(k)} = \int_0^\infty t^{k-1} \exp(-t)\, dt \tag{9}$$

is the gamma function. The mean value is given by k/θ. Note that Gamma distributions generalize Erlang distributions to

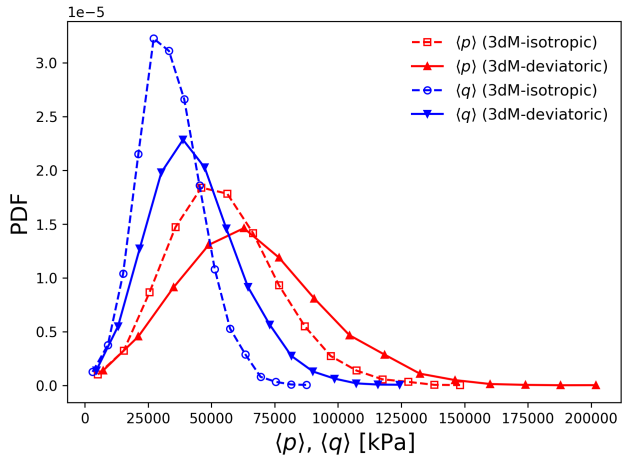

(a) PDFs of the center $\langle p \rangle$ and radius $\langle q \rangle$ of Mohr's circles

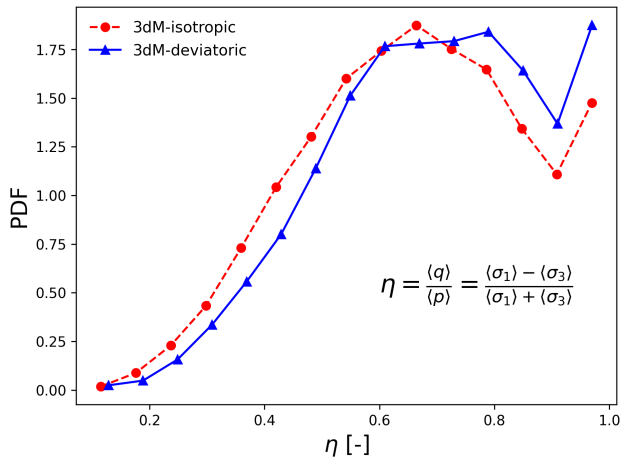

(b) PDF of the failure ratio η

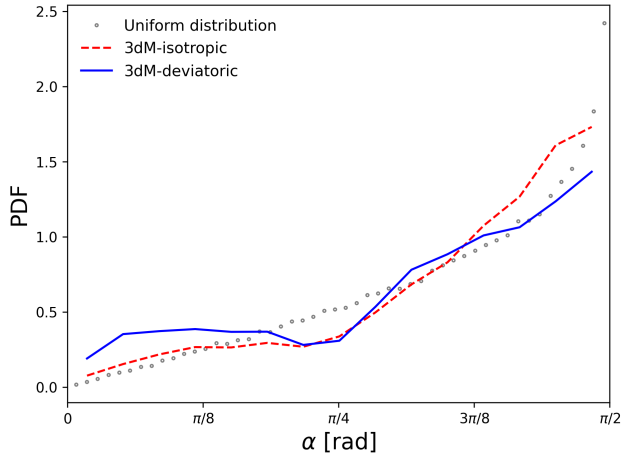

(c) PDF of the orientation of the major principal stress (angle θ between the direction of the major principal stress and that of the deviatoric compression)

Fig. 8. Non-normalized PDFs of the stresses on the microscale under isotropic and deviatoric stress conditions

non-integer shape parameter values and that the exponential distribution is a particular case of the Erlang distribution with shape parameter $k = 1$ Forbes *et al.* (2011).

Figures 9 and 10 suggest that, for practical purposes, the PDFs of microscale average normal stresses can be approximated by Gamma distributions of shape parameter

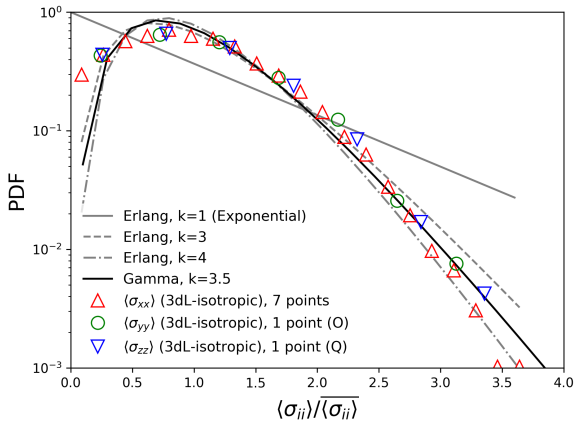

Fig. 9. Normalized PDFs of the average normal stress obtained on the microscale from a packing made of 3375 particles subjected to isotropic compression, measured from several sizes of statistical samples

$k \sim 3.5$ and scale parameter $\theta \sim 3.5/\sigma_{ii}$. This approximation underestimates the PDF at low values and overestimates the probability of finding values around the mean value. It is also clear that the Gamma distribution, which falls to zero at the origin is not a good match for the stresses caused by weak forces. Despite this limitation, the use of Gamma distributions is useful to understand the variability of stresses at the mesoscale.

The reasonable performance of the proposed approximation is also evidenced by the results obtained when comparing the different principal stresses, isotropic and deviatoric compression states, samples involving different numbers of particles or quasi monodispersed and polydispersed samples (Fig. 10). Note that for clarity of the figure, only a few data series are presented to illustrate each of the following results:

a) The PDFs of normalized microscale average normal stress are similar along all principal directions. This is shown for samples under isotropic loading in Fig. 10a and for samples under either isotropic or deviatoric loading in Fig. 10b.
b) There is no scale effect as the same normalized microscale average normal stress PDF is found for the large (3dL) and small (3dS) samples, involving, respectively, 3375 and 343 particles (Fig. 10c).
c) There is no appreciable difference between the normalized microscale average normal stress PDFs obtained from 2D and 3D models (Fig. 10c).

When the grain size distribution is less uniform (*i.e.* for the polydisperse system) the Gamma distributions offer a weaker match (Fig. 10d, however a Gamma distribution with $k = 3.5$ still offers a reasonable approximation, particularly in the range of over-average microscale stress. This seems reasonable, as the sum of independent exponential distributions generates Erlang distributions and the magnitude of large forces is exponentially distributed. Clearly, this reasoning is incomplete, as Eq. 1 indicates that both magnitude and orientation of contact force contribute to microscale stress. However, it is plausible that the effects of local fabric are small when large contact forces are in play and more significant when only lower forces are present, which will be the case for the lower values of microscale stress which, as noted, are those that depart more significantly from the fitting distribution.

Fig. 11 shows the normalized PDF of shear stresses gathered from 3dL experiments. Data are collected both for isotropic

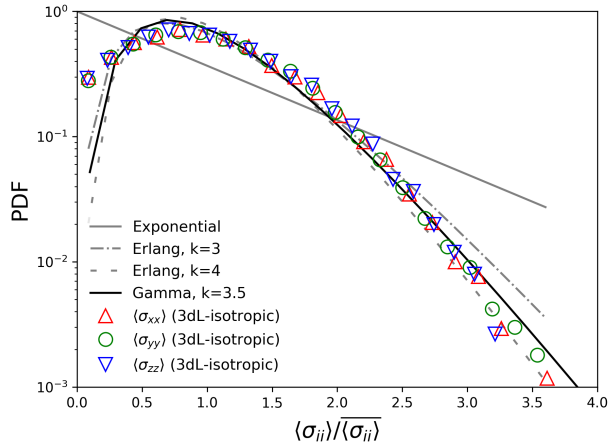

(a) Normal components of the stress under isotropic compression

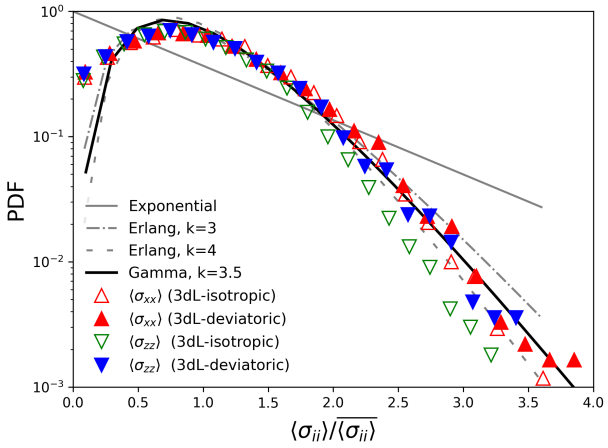

(b) Isotropic *vs.* triaxial compression states

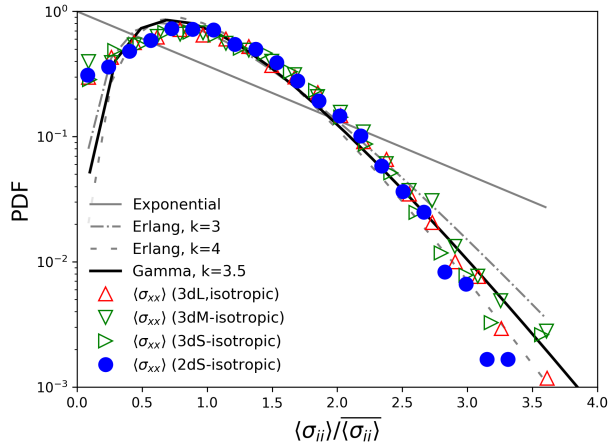

(c) 2D and 3D packings made of 324 (2d), 343 (3dS) and 3375 (3dL) under isotropic compression

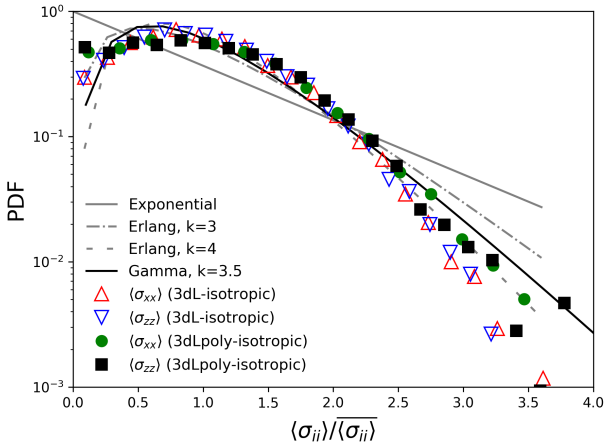

(d) Monodispersed *vs.* polydispersed packings under isotropic compression

Fig. 10. Normalized PDFs of normal stresses measured on the microscale

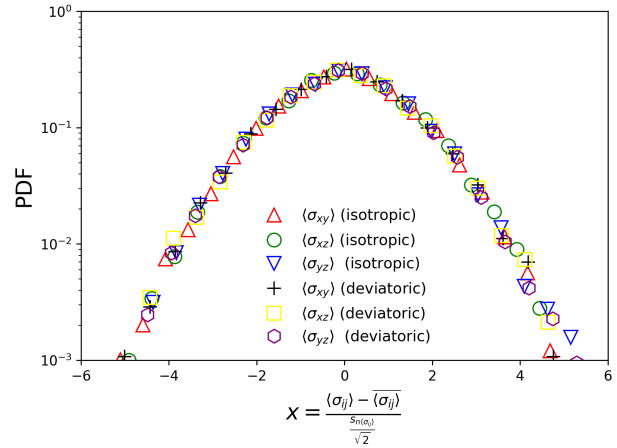

Fig. 11. Normalized PDFs of shear stress under isotropic and deviatoric compression measured on the microscale.

and deviatoric compression conditions: the different stress condition makes no noticeable difference to the normalized PDFs. The sample mean and standard deviation of the 3dL series are shown in Table 4. As expected, as no boundary shear stress are applied, the sample means are all close to 0. Interestingly, the standard deviations are not null but of the same order of magnitude of those for the distributions of normal stresses. That random microscale variability is slightly increased by the presence of a macroscopic deviatoric stress.

Table 4. Normal and shear stressses measured in the 3dL triaxial experiments

Microscale stress [kPa]	Isotropic compression $\overline{\langle\sigma_{ij}\rangle}$	Isotropic compression $s_{\mathcal{N}\langle\sigma_{ij}\rangle}$	Deviatoric compression $\overline{\langle\sigma_{ij}\rangle}$	Deviatoric compression $s_{\mathcal{N}\langle\sigma_{ij}\rangle}$
$\langle\sigma_{xx}\rangle$	50.46	29.05	50.42	30.21
$\langle\sigma_{yy}\rangle$	50.85	29.11	50.84	30.23
$\langle\sigma_{zz}\rangle$	50.83	29.19	78.59	46.95
$\langle\sigma_{xy}\rangle$	0.19	16.12	0.04	16.79
$\langle\sigma_{xz}\rangle$	0.24	16.24	0.20	21.70
$\langle\sigma_{yz}\rangle$	0.05	16.26	−0.04	21.56

Mesoscale stress variation

The mesoscale stress, *i.e.*, the average stress field within a control region R_N including N particles is given by:

$$\left\langle\left\langle\sigma_{ij}\right\rangle\right\rangle^{\mathrm{R}_N} = \frac{\sum_{m=1}^{N}\left\langle\sigma_{ij}\right\rangle^{m} V^m}{\sum_{m=1}^{N} V^m}, \tag{10}$$

where $\langle\sigma_{ij}\rangle^m$ is the average stress field within the Voronoi cell associated to particle m and V^m is the volume of this cell.

The PDF of mesoscale stress may be deduced from that of microscale stress. As noted above it is approximate enough to assume that the microscale stress $\langle\sigma_{ii}\rangle$ follows a Gamma distribution of shape parameter $k = 3.5$ and scale parameter $\theta = 3.5/\sigma_{ii}$, *i.e.*,

$$\langle\sigma_{ii}\rangle \sim \Gamma_{\left(3.5,\frac{3.5}{\sigma_{ii}}\right)}, \tag{11}$$

Gamma functions with the same scale parameter are additive in the shape parameter. That is, if $X \sim \Gamma_{(k_1,\theta)}$ and $Y \sim \Gamma_{(k_2,\theta)}$ then:

$$X + Y \sim \Gamma_{(k_1+k_2,\theta)}. \tag{12}$$

Therefore, for a control region R_N that includes N particles, assuming that Voronoi average stresses are independent, neglecting differences in volume V^m between Voronoi cells and the effect of rattlers, because of Eq. 10 the PDF of stresses on the mesoscale would be:

$$\langle\langle\sigma_{ii}\rangle\rangle^{\mathrm{R}_N} \sim \Gamma_{\left(3.5N,\frac{3.5N}{\sigma_{ii}}\right)}, \tag{13}$$

i.e., a Gamma distribution of shape parameter $k = 3.5N$ and scale parameter $\theta = 3.5N/\sigma_{ii}$.

The expected value of the normal stress on the mesoscale would be $\mu_{\langle\langle\sigma ii\rangle\rangle^{\mathrm{R}_N}} = \sigma_{ii}$ and the standard deviation would be $\sigma_{\langle\langle\sigma_{ii}\rangle\rangle^{\mathrm{R}_N}} = \sigma_{ii}/\sqrt{kN}$. The coefficient of variation of the mesoscale stress is thus

$$CoV_{\langle\langle\sigma_{ii}\rangle\rangle^{\mathrm{R}_N}} = \frac{\sigma_{\langle\langle\sigma_{ii}\rangle\rangle^{\mathrm{R}_N}}}{\mu_{\langle\langle\sigma_{ii}\rangle\rangle^{\mathrm{R}_N}}} = \frac{1}{\sqrt{kN}}, \tag{14}$$

irrespective of the value of σ_{ii} (*i.e.* independently of the macroscopic stress field).

Equation 14 assumes that the number of particles in the control region does not change from one realization to another. However this is not necessarily true, especially when samples are poly-dispersed or when control regions are small. As a result, the variability of the joint PDF can be different. In addition, the stresses on the microscale do not follow exactly Gamma distributions and the control region could include some rattlers so that the variability of the stress on the mesoscale may be higher than what Eq. 14 is predicting. As a simple correction measure, k can be replaced by k^* (with $k^* < k$), a new parameter to be callibrated from experiments (as explained below):

$$CoV_{\langle\langle\sigma_{ii}\rangle\rangle^{\mathrm{R}_N}} = \frac{1}{\sqrt{k^*N}}. \tag{15}$$

For practical purposes, k can be obtained from the PDF of the stressess on the microscale (*i.e* stresses measured on samples of Voronoi cells associated to particles under the same macroscopic stress conditions) whereas k^* can be obtained from the variability of the stress field measured within a control region that includes 1 particle on average (R_1).

$$k = \left(CoV_{\langle\sigma_{ii}\rangle}\right)^{-2} \tag{16}$$

and

$$k^* = \left(CoV_{\langle\langle\sigma_{ii}\rangle\rangle^{\mathrm{R}_1}}\right)^{-2}. \tag{17}$$

The approximate expression given by Eq. 15 can be contrasted with the results of the numerical experiments. We generated statistical samples of mesoscale stresses measured within several control regions. The sample mean and sample standard deviation are used to estimate the coefficient of variation as:

$$CoV_{\langle\langle\sigma_{ii}\rangle\rangle^{\mathrm{R}_N}} = \frac{s_{\mathcal{N}\langle\langle\sigma_{ii}\rangle\rangle^{\mathrm{R}_N}}}{\overline{\langle\langle\sigma_{ii}\rangle\rangle^{\mathrm{R}_N}}}. \tag{18}$$

In Fig. 12 we plot the relationship between $CoV_{\langle\langle\sigma_{ii}\rangle\rangle^{\mathrm{R}_N}}$ of the normal stresses (in the three principal directions x, y and z) and the number of particles N included within each control region in quasi monodispersed (small, medium and large models) and polydispersed samples. These data are compared to those predicted by Eq. 15. The value of k^* is obtained from the variability of the stress within a control region including 1 particle on average. Eq. 14 with a value of k obtained from the variability of stresses on the microscale is also plotted. The differences between both approximations are explained by the missmatching between the PDFs of stresses on the microscale and Gamma distributions, because of the variability of the number of particles found within each control region (Fig. 12c) and the presence of the rattlers. The trend observed in the set of numerical experiments is reproduced by the model. A limit between meso- and macroscales can be set after agreeing a maximum acceptable value of stress variability, as expressed through the $CoV_{\langle\langle\sigma_{ii}\rangle\rangle^{\mathrm{R}_N}}$. For example, for quasi monodispersed samples, the limit $CoV_{\langle\langle\sigma_{ii}\rangle\rangle^{\mathrm{R}_N}} < 0.01$ would require $N \gtrsim 6600$.

EXAMPLE APPLICATIONS

Variability in simulated cone tip resistance

Having an explicit approximate expression to describe the variability of the stress field on the mesoscale facilitates the interpretation and treatment of geotechnical problems where the granular mesoscale is relevant. As a first example consider the set of numerical cone penetration test experiments Butlanska (2014) represented in Figure 13. The relationship between the cone tip resistance q_p [MPa] and the penetration depth z [m] is fitted through the following expression:

$$q_\mathrm{p} = a\left(1 - \exp\left(-bz\right)\right), \tag{19}$$

where a [MPa] and b [m^-1] are fitting parameters. This expression means that the cone tip resistance progressively tends towards the value a, which can be considered as the stationary cone tip resistance. The parameter b sets the rate at which the stationary cone resistance is approached and may be applied to select the depth range for which the steady state is relevant, for instance $q_\mathrm{p} > 0.9a$ when $z > -\ln(0.1)/b$. Arroyo *et al.* (2011) argued that the reduction on cone tip resistance variability around the trend demonstrated in the results reflected the reducing cone diameter (d_c) to median particle size (D_{50}) ratio, n_p. The number of particles in contact with the cone tip was continuously measured, presenting a CoV_N that ranged between 0.111 ($n_\mathrm{p} = 2.69$, $D_\mathrm{R} = 75\%$) and 0.036 ($n_\mathrm{p} = 8.06$, $D_\mathrm{R} = 90\%$) Butlanska (2014). Using the statistics of mesoscale stress, it is now possible to evaluate this effect without the need for lengthy simulations. The variability of measured cone tip resistance, CoV_{q_p} should be closely related to the variability of the average mesoscale stress in the region contacting the cone tip, $CoV_{\langle\langle\sigma_{ii}\rangle\rangle^{\mathrm{R}_N}}$, although there are other effects that should be taken into account (*e.g.* stress conditions different from triaxial compression, specific stress transmission patterns induced by the cone tip, etc.).

The coefficient of variation of simulated cone tip resistance at steady state computed from the simulations of Butlanska (2014) is compared to the estimation obtained from Eq. 15 for a given average number of particles in contact with the cone (Fig. 14). The best fitting values for k^* are in the range $2.6 - 2.7$. The comparison of the values obtained from

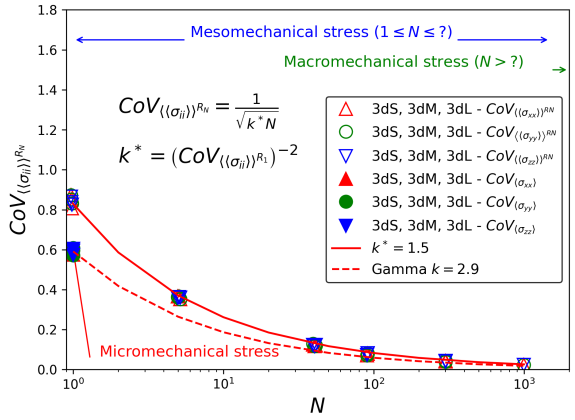

(a) Variability of the mesoscale stress with quasi monodispersed samples

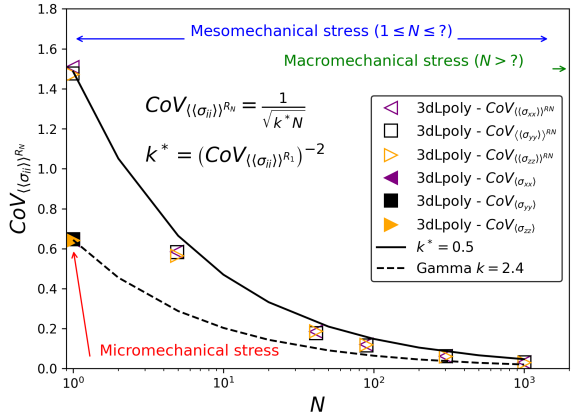

(b) Variability of the mesoscale stress with polydispersed samples

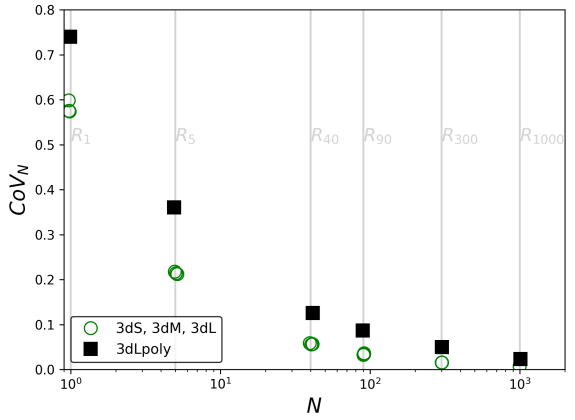

(c) Variability of the number of particles included within each control region

Fig. 12. Variability of the coefficient of variation of the normal stress and number of particles included in the control regions. The data obtained from the numerical experiments are compared to the proposed model with several values of k and k^*.

DEM simulations with the theoretical variability curve is quite satisfactory, reproducing to a large extent the decay of CoV_{q_p} from the expected decay of $CoV_{\langle\langle\sigma_{ii}\rangle\rangle^{R_N}}$ with the number of particles in contact with the cone tip.

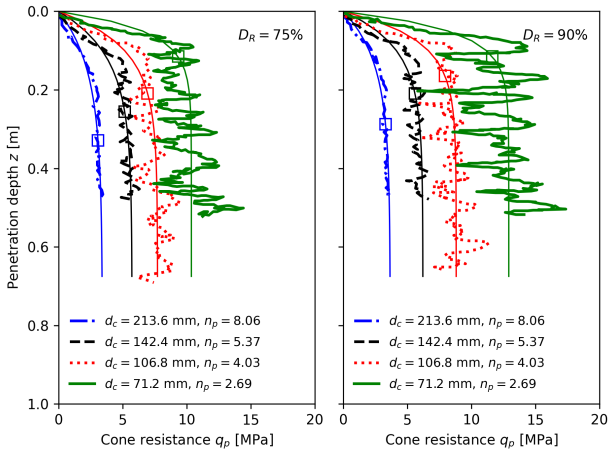

Fig. 13. Tip cone resistance measured in a virtual chamber cone penetration test for two different relative densities D_R and different cone diameter to median particle size ratios, n_p (after Butlanska (2014)). The exponential curve fitting to each curve is also presented, with square markers indicating the depth in which the fitted curve attains 90% of its steady state value

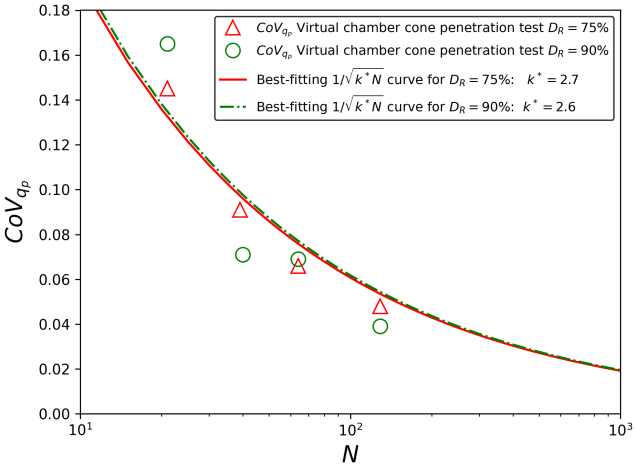

Fig. 14. Comparison of the CoV measured in virtual chamber cone penetration tests by Butlanska (2014) with the values expected from Gamma distributions whose shape parameters are obtained from least squares fitting

Variability of stress-cell measurements in granular soils

Mesoscale effects are present when considering stress-cell measurements in granular soils. The question of how the particle to cell size ratio affects stress-cell measurements has been addressed experimentally in studies of stress cells based on different measurement principles Weiler & Kulhawy (1982); Miura *et al.* (2003); Kootahi & Leung (2022). Kootahi & Leung (2022) investigated the effects of soil particle size on the measurement accuracy of single-point type tactile pressure sensors. Sensors with two different diameters were integrated into oedometer cells and 9 different levels of stress were applied in order to understand the influence of the sensor to particle size ratio on measurement error. In the work of Kootahi & Leung (2022) the mean absolute percentage errors of repeated sensor measurements, $MAPE$, were reported. The $MAPE$ is defined as:

$$MAPE = \frac{1}{\mathcal{N}} \sum_{n=1}^{\mathcal{N}} \left| \frac{p_{\text{oed}} - \sigma_n}{p_{\text{oed}}} \right|, \tag{20}$$

where p is the oedometric cell pressure and σ_n is the stress measured by the sensor in realization n and $\mathcal{N}$ is the number of measurements. The experimental results obtained were summarized by the following empirical expression:

$$MAPE = \exp\left(0.69 + \frac{9.76}{d_s/D_{50}}\right), \tag{21}$$

where d_s is the sensor diameter and D_{50} the mean grain size of the soil. The expression clearly conveys that measurement error is reduced as the ratio of sensor size to mean grain size increases. That ratio may be also employed to estimate the number of particles in contact with the sensor since, assuming a relevant cylindrical volume of height D_{50} above the sensor,

$$N = \frac{3}{2}\left(\frac{d_s}{D_{50}}\right)^2 (1-n)\,. \tag{22}$$

The expressions above (Eqs. 21 and 22) can be easily combined to express $MAPE$ as a function of the number of particles in contact with the sensor, as shown in Fig. 15.

This experimental result may be compared with predictions based of mesoscale variability. To this end the stress cell sensor measurement outputs from the oedometer may be simulated using a Monte Carlo method. The procedure involves several steps:

1. sample a large number -say w- of microscale stress values from a relevant distribution -for instance a Gamma of parameters k and $\theta = k/p_{\text{oed}}$, where p_{oed} is the applied oedometric pressure, or from the statistical sample gathered from the DEM simulations,
2. resampling, with a number of repeats given by $\mathcal{N}$, smaller N-sized subsets from the generated population, for instance with $\mathcal{N} = 1000$ repeats
3. computing for each N-sized microscale stress subset the average stress value, which is equivalent to a stress cell measurement, σ_i
4. computing $MAPE$ as per Eq. 20, averaging the normalized error for the $\mathcal{N}$ subsamples of size N.

The results of this numerical experiment, run for $w = 10^5$, $\mathcal{N} = 10^3$ and $k = 3.5 - 4.5$ are also presented in Figure 15. In the particle number range ($N > 25$, equivalent to $D_s/D_{50} > 8$) the comparison between the simulated and experimental results is very good, particularly for the distribution with parameter $k = 2.5$. At large particle numbers the experimental results approach an asymptote and lie somewhat above the simulation: this may be related by other sources of error in the experiment, such as instrument resolution. The tactile sensors are based on the reduction of the electric resistance caused by the creation of conductive paths as the force pads are uniformly compressed. However, with a low number of particles the load is not uniformly distributed and it is likely that the assumed electrical transduction principle is also affected (incrasing the $MAPE$).

DISCUSSION

It is of some interest to consider how general the mesoscale variability backbone found here (Figure 12) may be. This is tentatively explored in this section, first with relation to stress and then with respect to other variables.

The exact shape of the microscale stress distribution that serves as base for the mesoscale variability transition backbone is given by parameter k^*. For the applications examined above it has become apparent that, on the microscale, the k-values between 2.5 and 3.5 that were inferred from the numerical experiments offer good approximation. This is in contrast

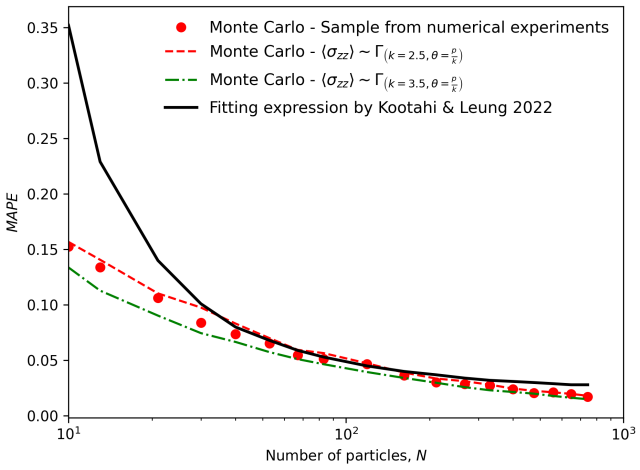

Fig. 15. Comparison of the $MAPE$ measured from Monte Carlo simulations with the equation proposed by Kootahi & Leung (2022) to fit experimental data

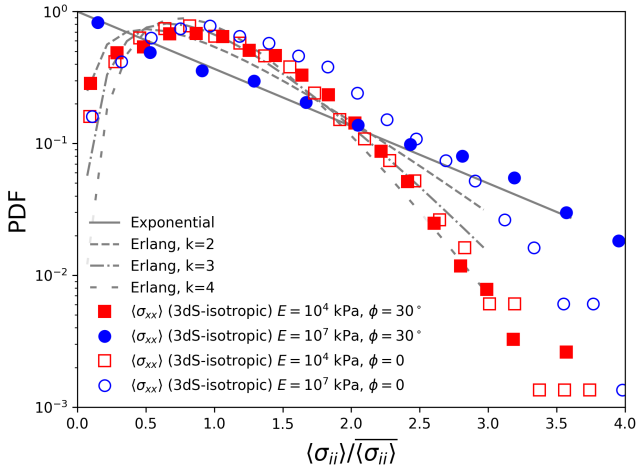

Fig. 16. Sensitivity of microstress PDF to contact parameters

with results from Tejada (2020), who extracted microscale stress distributions from DEM simulations of a strip foundation problem observing k-values between 1 and 2. There are several important differences between the DEM models examined in this work and those in Tejada (2020). In Tejada (2020) a) the applied boundary conditions were not homogeneous, b) sample generation took place under gravity c) contact stiffness was very high, 10^3 times higher than the one applied here. This last trait was suspected to be the more influent and a check was carried out by repeating the 3dS set of simulations with increased contact stiffness. The result, shown in Figure 16, confirms that a large increase in contact stiffness widens the microscale stress distribution. A separate check, also shown in Figure 16, was carried out on interparticle friction, which appeared to have much lesser effect on the microscale stress PDFs. Very high contact stiffness values in DEM are more appropriate for artificial granular materials such as steel or glass Suhr & Six (2016) than for soils, where grain contact stiffness is significantly lowered by roughness Otsubo *et al.* (2015). Nevertheless, the results indicate that further research is needed to clarify the factors controlling the precise value of the scaling parameter k^* that may apply for a particular material. Factors to explore should include grain shape, which has a complex effect on test repeatability Adesina *et al.* (2022).

Note that, as long as the microscale stress distribution fits into the Gamma / Erlang family, the mesoscale stress variability transition backbone (Eq. 14) would still be valid, even though the shape parameter k^* may vary.

The situation is far more complex if other properties beyond stress are considered (*e.g.* porosity, stiffness, strength). When going towards the mesoscale, a general observation from similar DEM studies (*e.g.* Kuhn & Bagi (2009); Tejada & Antolin (2021); Adesina *et al.* (2022); Leak & Barreto (2023) is that the range of variation of soil behaviour always reduces with an increase in both specimen size N and number of simulations. This may be understood as a consequence of of the law of large numbers. In principle, every quantity may scale its variability with sample size in a different way, as a) the underlying microscale quantity relevant in each case -the equivalent to microscale stress here- may be different b) the PDF of that relevant microscale distribution may be different than a Gamma or Erlang function c) the role of different microscale properties (particle shape, contact stiffness, etc) may be also different. It is not thus clear *a priori* if the mesoscale transition will be faster or slower than that of stress for any given property. However, because of the central limit theorem, if the PDF of a given microscale quantity x has a finite variance σ_x, when averaging over a volume that includes N particles, then the coefficient of variation is given by

$$CoV_{\langle x\rangle^{\mathrm{R}_N}} = \frac{\sigma_{\langle x\rangle^{\mathrm{R}_N}}}{\mu_{\langle x\rangle^{\mathrm{R}_N}}} = \frac{CoV_{\langle x\rangle^{\mathrm{R}_1}}}{\sqrt{N}}, \tag{23}$$

where $CoV_{\langle x\rangle^{\mathrm{R}_1}}$ is the coefficient of variation of x for a region containing 1 particle on average. Indeed, Eq. 23 is a generalization of the backbone curve proposed herein to assess the variability of stresses on the mesoscale (Eq. 14), since $CoV_{\langle\langle\sigma_{ii}\rangle\rangle^{\mathrm{R}_1}} = 1/\sqrt{k^*}$ for normal stresses. Actually, there are some examples corroborating the approach presented by Equation 23. For example, the DEM simulations of drained triaxial compression of loose samples Tejada & Antolin (2021) (which showed that the coefficient of variation of the tangent elastic modulus, CoV_{E_0} , was not below 0.05 in granular packings involving less than 10^5 particles). On the other hand, Leak & Barreto (2023) presented results from which the effect of sample size on the measure of initial void ratio e_0 in DEM packings could be inferred. Finally, Kuhn & Bagi (2009) focused on the variability of the normalized strength and Young's modulus of granular packings with the number of particles involved in them. These results (Figure 17) showed a similar scaling of variability with particle number to that observed here (*i.e.* $CoV \propto 1/\sqrt{N}$), although indicating different variabilities for a given particle number. The coefficient of determination $\mathcal{R}^2$ was over 0.99 for e_0, E^{norm} and q^{norm} and over 0.93 for E_0 and q^{ult}. The reason for a worse fitting in the latter is the number of repeats (only 15 for each number of particles, much lower than in the numerical experiments of Leak & Barreto (2023) and Kuhn & Bagi (2009)).

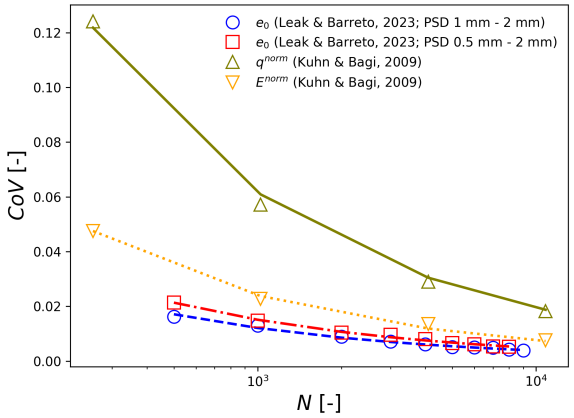

(a) Initial void ratio Leak & Barreto (2023), normalized strength and normalized Young's modulus Kuhn & Bagi (2009) (observed values and best-fitting curves defined by Eq. 23)

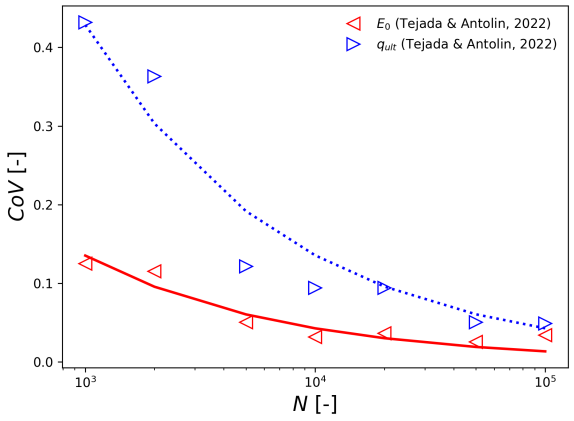

(b) Tangent modulus E_0 and threshold stress q_{ult} Tejada & Antolin (2021) (observed values and best-fitting curves defined by Eq. 23)

Fig. 17. Variation of the coefficient of variation of several macroscopic quantities on the mesoscale with the specimen size (number of particles N)

CONCLUSION

We performed several series of numerical experiments of triaxial compression of granular samples made of quasi monodispersed and polydispersed spheres. The stress was measured on the microscale (*i.e.* average stress of the nearest particle-associated volume space to some control point) and on the mesoscale (*i.e.* average stress field within regions including from a single to a few hundred particles on average.

The statistical distributions of normal stresses on the microscale could be approximated for practical purposes by Gamma distributions of shape parameter $k \sim 3.5$ and scale parameter defined by the external stress field $\theta = k/\sigma_{ii}$. The PDFs of micromechanical stresses did not show significant differences when comparing isotropic and deviatoric compression, 2D or 3D problems and smaller or larger particles. The missmatching between the observed PDFs and Gamma distributions is more noticeable with polydispersed packings.

When focusing on the mesoscale, Gamma distributions can be used as well. In these cases, the variability is expected to decrease significantly with the number of particles as $CoV_{\langle\langle\sigma_{ii}\rangle\rangle^{\mathrm{R}_N}} \sim 1/\sqrt{k^* N}$ with $k^* = 1.5$ for monodispersed samples and $k^* = 0.5$ for polydispersed samples. This expression means that the variability of the stress is independent of the stress applied but it just depends on the number of particles involved. The CoV can be used as an estimator of the variability of the stress field on the mesoscale. Limiting its value can serve as an agreed definition of the macroscale and hence may be used as an objective measure to define a representative volume element.

Understanding the relationship between the stress variability and the number of particles can explain, for example, the expected errors when using tactile stress sensors and coarse

particles or why the cone resistance measured in a virtual chamber cone penetration tests fluctuates around a given value when the size of particles is not so far from the cone or sensor diameter.

The mesoscale transition concept may be of application to other macroscopic quantities or mechanical properties different from stress. The exact form that the transition backbone curves may take in each case is a worthy subject for further research.

ACKNOWLEDGMENTS

Financial support of Ministerio de Ciencia e Innovación of Spain (MCIN/AEI/10.13039/501100011033) through research project PID2020-119598RB-I00 is gratefully appreciated.

COMPETING INTERESTS

The authors declare that there is no conflict of interest.

DATA AVAILABILITY

Data generated or analyzed during this study are available from the corresponding author upon reasonable request.

NOTATION LIST

a, b	fitting parameters for cone tip resistance
CoV_x	coefficient of variation of x
D	particle diameter
D_{50}	median particle size
D_{R}	relative density
d_{c}	cone diameter
d_{s}	sensor diameter
E	Young's modulus of particles
E_0	tangent elastic modulus of a granular packing
E^{norm}	normalized Young's modulus of a granular packing
e_0	initial void ratio
$\mathbf{F}_{\mathrm{n}}^{mn}$	normal interaction force between particles m and n
$\mathbf{F}_{\mathrm{s}}^{mn}$	tangential interaction force between particles m and n
k	shape parameter in Gamma distributions
k^*	parameter scaling the variability on the mesoscale
k_{n}	normal stiffness
k_{s}	tangential stiffness
l	size of the simulation box
$MAPE_x$	mean absolute percentaje error of x
N	number of particles
$\mathcal{N}$	number of realizations of an experiment
N_{c}	coordination number of a packing
n	porosity
n_{p}	cone diameter to median particle size ratio
O, P, Q	control points
p	isotropic compression stress
p_{oed}	oedometric compression stress
q	half deviatoric stress (radius of Mohr's circle)
q^{norm}	normalized strength of a granular packing
q^{ult}	ultimate strength of a granular packing
q_{p}	cone tip resistance
R_N	control region containing N particles on average
R^m	particle radius
$\mathcal{R}^2$	coefficient of determination
r	proportion of rattlers in a packing
$\mathbf{r}^m$	absolute position vector
$\mathbf{r}^{mn}$	relative position vector
$s_{\mathcal{N}x}$	sample standard deviation of variable x
u^{mn}	lateral displacement between particles m and n
V^m	volume of Voronoi cell associated to particle m
w	size of the sample space
X	generic variable
Y	generic variable
x	generic variable
$\bar{x}$	sample mean of x
z	penetration depth of the cone tip
α	orientation angle of micromechanical major stresses
δ^{mn}	overlap between particles m and n
ε_{ij}, ε_I	macroscopic strain field
$\Gamma_{(k)}$	Gamma function
η	failure ratio
μ_x	mean value of variable x
ϕ	interparticle friction angle
ρ	Pearson correlation coefficient
Σ_{ij}^m	extensive stress field of Voronoi cell m
σ_{ij}, σ_I	macroscopic stress field
σ_{ij}^m	stress field within Voronoi cell m
$\langle\sigma_{ij}\rangle^m$	average stress over Voronoi cell m
$\langle\langle\sigma_{ij}\rangle\rangle^{\mathrm{R}_N}$	average stress over a mesoscopic region
σ_x	standard deviation of variable x
θ	scale parameter of Gamma distribution

REFERENCES

Adesina, P., O'Sullivan, C., Morimoto, T. & Otsubo, M. (2022). Determining a representative element volume for dem simulations of samples with non-circular particles. *Particuology* **68**, 29–43, doi:https://doi.org/10.1016/j.partic.2021.10.007.

Alabbasi, Y. & Hussein, M. (2021). Geomechanical modelling of railroad ballast: A review. *Archives of Computational Methods in Engineering* **28**, No. 3, 815–839, doi:10.1007/s11831-019-09390-4.

Alonso, E. E., Tapias, M. & Gili, J. (2012). Scale effects in rockfill behaviour. *Géotechnique Letters* **2**, No. 3, 155–160, doi:10.1680/geolett.12.00025.

Antony, S. J. (2000). Evolution of force distribution in three-dimensional granular media. *Phys. Rev. E* **63**, 011302, doi:10.1103/PhysRevE.63.011302, URL https://link.aps.org/doi/10.1103/PhysRevE.63.011302.

Arroyo, M., Butlanska, J., Gens, A., Calvetti, F. & Jamiolkowski, M. (2011). Cone penetration tests in a virtual calibration chamber. *Géotechnique* **61**, No. 6, 525–531, doi:10.1680/geot.9.P.067.

Bagi, K. (1996). Stress and strain in granular assemblies. *Mechanics of Materials* **22**, No. 3, 165 – 177, doi:http://dx.doi.org/10.1016/0167-6636(95)00044-5.

Balescu, R. (1975). Equilibrium and nonequilibrium statistical mechanics. *NASA STI/Recon Technical Report A* **76**.

Butlanska, J. (2014). Cone penetration test in a virtual calibration chamber .

Butlanska, J., Arroyo, M., Gens, A. & O'Sullivan, C. (2014). Multi-scale analysis of cone penetration test (cpt) in a virtual calibration chamber. *Canadian Geotechnical Journal* **51**, No. 1, 51–66, doi:10.1139/cgj-2012-0476.

Chareyre, B., Cortis, A., Catalano, E. & Barthélemy, E. (2012). Pore-scale modeling of viscous flow and induced forces in dense sphere packings. *Transport in Porous Media* **92**, No. 2, 473–493, doi:10.1007/s11242-011-9915-6.

Ciantia, M., Arroyo, M., Calvetti, F. & Gens, A. (2015). An approach to enhance efficiency of dem modelling of soils with crushable grains. *Géotechnique* **65**, No. 2, 91–110, doi:10.1680/geot.13.P.218.

Ciantia, M., Arroyo, M., Calvetti, F. & Gens, A. (2016a). A numerical investigation of the incremental behavior of crushable granular soils. *International Journal for Numerical and Analytical Methods in Geomechanics* **40**, No. 13, 1773–1798, doi:https://doi.org/10.1002/nag.2503.

Ciantia, M. O., Arroyo, M., Butlanska, J. & Gens, A. (2016b). Dem modelling of cone penetration tests in a double-porosity crushable granular material. *Computers and Geotechnics* **73**, 109–127, doi:10.1016/j.compgeo.2015.12.001.

Ciantia, M. O., Arroyo, M., O'Sullivan, C., Gens, A. & Liu, T. (2019). Grading evolution and critical state in a discrete numerical model of fontainebleau sand. *Géotechnique* **69**, No. 1, 1–15, doi:10.1680/jgeot.17.P.023.

Ciantia, M. O., Boschi, K., Shire, T. & Emam, S. (2018). Numerical techniques for fast generation of large discrete-element models. *Proceedings of the Institution of Civil Engineers - Engineering and Computational Mechanics* **171**, No. 4, 147–161, doi:10.1680/jencm.18.00025.

Coppersmith, S. N., h. Liu, C., Majumdar, S., Narayan, O. & Witten, T. A. (1996). Model for force fluctuations in bead packs. *Phys. Rev. E* **53**, 4673–4685, doi:10.1103/PhysRevE.53.4673.

Cundall, P. A. (1987). Distinct element models, of rock and soil structure. *Analytical and Computational Method in Engineering Rock Mechanics* , 129–163I.

Cundall, P. A. & Strack, O. D. L. (1979). A discrete numerical model for granular assemblies. *Géotechnique* **29**, No. 1, 47–65, doi:10.1680/geot.1979.29.1.47.

Drescher, A. & de Josselin de Jong, G. (1972). Photoelastic verification of a mechanical model for the flow of a granular material. *Journal of the Mechanics and Physics of Solids* **20**, No. 5, 337–340, doi:10.1016/0022-5096(72)90029-4, cited By 438.

Edwards, S. (2005). The full canonical ensemble of a granular system. *Physica A* **353**, 114–118.

Edwards, S., Grinev, D. & Brujić, J. (2003). Fundamental problems in statistical physics of jammed packings. *Physica A* **330**, 61–76.

Edwards, S. & Oakeshott, R. (1989). Theory of powders. *Physica A* **157**, No. 3, 1080–1090.

Forbes, C., Evans, M., Hastings, N. & Peacock, B. (2011). *Statistical distributions*. Wiley.

Frossard, E., Hu, W., Dano, C. & Hicher, P.-Y. (2012). Rockfill shear strength evaluation: a rational method based on size effects. *Géotechnique* **62**, No. 5, 415–427, doi:10.1680/geot.10.P.079.

h. Liu, C., Nagel, S. R., Schecter, D. A., Coppersmith, S. N., Majumdar, S., Narayan, O. & Witten, T. (1995). Force fluctuations in bead packs. *Science* **269**, No. 5223, 513–515, doi:10.1126/science.269.5223.513.

Henkes, S. & Chakraborty, B. (2009). Statistical mechanics framework for static granular matter. *Phys. Rev. E* **79**.

Henkes, S., Hern, C. S. O. & Chakraborty, B. (2007). Entropy and temperature of a static granular assembly: An ab initio approach. *Phys. Rev. Lett.* **99**, No. 3, 1–4.

Jaeger, H. M. & Nagel, S. R. (1996). Granular solids, liquids, and gases. *Reviews of Modern Physics* **68**, No. 4, 1259–1271.

Kikumoto, M., Wood, D. M. & Russell, A. (2010). Particle crushing and deformation behaviour. *Soils and Foundations* **50**, No. 4, 547–563, doi:https://doi.org/10.3208/sandf.50.547.

Kootahi, K. & Leung, A. K. (2022). Effect of soil particle size on the accuracy of tactile pressure sensors. *Journal of Geotechnical and Geoenvironmental Engineering* **148**, No. 10, 06022008, doi:10.1061/(ASCE)GT.1943-5606.0002899.

Kozicki, J., Tejchman, J. & Mühlhaus, H.-B. (2014). Discrete simulations of a triaxial compression test for sand by DEM. *International Journal for Numerical and Analytical Methods in Geomechanics* **38**, No. 18, 1923–1952, doi:10.1002/nag.2285.

Kuhn, M. R. & Bagi, K. (2009). Specimen size effect in discrete element simulations of granular assemblies. *Journal of Engineering Mechanics* **135**, No. 6, 485–492, doi:10.1061/(ASCE)0733-9399(2009)135:6(485).

Larese, A., Rossi, R., Oñate, E., Ángel Toledo, M., Morán, R. & Campos, H. (2015). Numerical and experimental study of overtopping and failure of rockfill dams. *International Journal of Geomechanics* **15**, No. 4, 04014060, doi:10.1061/(ASCE)GM.1943-5622.0000345.

Leak, J. & Barreto, D. (2023). A dem study on the effect of inherent variability of assemblies of spherical particles. In *Proceedings 10th NUMGE 2023: 10th European Conference on Numerical Methods in Geotechnical Engineering*, doi:10.53243/NUMGE2023-388.

Løvoll, G., Måløy, K. J. & Flekkøy, E. G. (1999). Force measurements on static granular materials. *Phys. Rev. E* **60**, 5872–5878, doi:10.1103/PhysRevE.60.5872, URL https://link.aps.org/doi/10.1103/PhysRevE.60.5872.

Majmudar, T. S. & Behringer, R. P. (2005). Contact force measurements and stress-induced anisotropy in granular materials. *Nature* **435**, No. 7045, 1079–1082.

Mcdowell, G. R., Falagush, O. & Yu, H.-S. (2012). A particle refinement method for simulating dem of cone penetration testing in granular materials. *Géotechnique Letters* **2**, No. 3, 141–147, doi:10.1680/geolett.12.00036.

Metzger, P. T. (2004). Granular contact force density of states and entropy in a modified edwards ensemble. *Phys. Rev. E* **70**, 051303, doi:10.1103/PhysRevE.70.051303.

Miura, K., Otsuka, N., Kohama, E., Supachawarote, C. & Hirabayashi, T. (2003). The size effects of earth pressure cells on measurement in granular materials. *Soils and Foundations* **43**, No. 5, 133–147, doi:https://doi.org/10.3208/sandf.43.5_133.

Mueth, D. M., Jaeger, H. M. & Nagel, S. R. (1998). Force distribution in a granular medium. *Phys. Rev. E* **57**, 3164–3169, doi:10.1103/PhysRevE.57.3164.

Ng, T.-T. (2004). Triaxial test simulations with discrete element method and hydrostatic boundaries. *Journal of engineering mechanics* **130**, No. 10, 1188–1194, doi:10.1061/(ASCE)0733-9399(2004)130:10(1188).

Nicot, F., Hadda, N., Guessasma, M., Fortin, J. & Millet, O. (2013). On the definition of the stress tensor in granular media. *International Journal of Solids and Structures* **50**, No. 14, 2508 – 2517, doi:10.1016/j.ijsolstr.2013.04.001.

Otsubo, M., O'sullivan, C., Sim, W. W. & Ibraim, E. (2015). Quantitative assessment of the influence of surface roughness on soil stiffness. *Géotechnique* **65**, No. 8, 694–700, doi:10.1680/geot.14.T.028.

Pathria, R. & Beale, P. (1996). *Statistical mechanics*. Elsevier Science.

Peters, J. F., Muthuswamy, M., Wibowo, J. & Tordesillas, A. (2005). Characterization of force chains in granular material. *Phys. Rev. E* **72**, 041307, doi:10.1103/PhysRevE.72.041307.

Radjai, F. (2015). Modeling force transmission in granular materials. *Comptes Rendus Physique* **16**, No. 1, 3 – 9, doi:https://doi.org/10.1016/j.crhy.2015.01.003, granular physics / Physique des milieux granulaires.

Radjai, F., Jean, M., Moreau, J.-J. & Roux, S. (1996). Force distributions in dense two-dimensional granular systems. *Phys. Rev. Lett.* **77**, 274–277, doi:10.1103/PhysRevLett.77.274.

Radjai, F., Roux, S. & Moreau, J. J. (1999). Contact forces in a granular packing. *Chaos: An Interdisciplinary Journal of Nonlinear Science* **9**, No. 3, 544–550, doi:10.1063/1.166428.

Salot, C., Gotteland, P. & Villard, P. (2009). Influence of relative density on granular materials behavior: DEM simulations of triaxial tests. *Granular matter* **11**, No. 4, 221–236, doi:10.1007/s10035-009-0138-2.

Shire, T. & O'Sullivan, C. (2016). Constriction size distributions of granular filters: a numerical study. *Géotechnique* **66**, No. 10, 826–839, doi:10.1680/jgeot.15.P.215.

Sibille, L., Donzé, F.-V., Nicot, F., Chareyre, B. & Darve, F. (2007). From bifurcation to failure in a granular material: a dem analysis. *Acta Geotechnica* **3**, No. 1, 15, doi:10.1007/s11440-007-0035-y.

Suhr, B. & Six, K. (2016). On the effect of stress dependent interparticle friction in direct shear tests. *Powder Technology* **294**, 211–220, doi:https://doi.org/10.1016/j.powtec.2016.02.029.

Taylor, H. F., O'Sullivan, C., Shire, T. & Moinet, W. W. (2019). Influence of the coefficient of uniformity on the size and frequency of constrictions in sand filters. *Géotechnique* **69**, No. 3, 274–282, doi:10.1680/jgeot.17.T.051.

Tejada, I. G. (2014). Ensemble theory for slightly deformable granular matter. *The European Physical Journal E* **37**, No. 9, 81, doi:10.1140/epje/i2014-14081-6.

Tejada, I. G. (2020). Stochastic approach to the solution of boussinesq-like problems in discrete media. *Journal of Elasticity* **141**, No. 2, 301–319, doi:10.1007/s10659-020-09785-6.

Tejada, I. G. & Antolin, P. (2021). Use of machine learning for unraveling hidden correlations between particle size distributions and the mechanical behavior of granular materials. *Acta Geotechnica* doi:10.1007/s11440-021-01420-5.

Tejada, I. G., Sibille, L. & Chareyre, B. (2016). Role of blockages in particle transport through homogeneous granular assemblies. *EPL (Europhysics Letters)* **115**, No. 5, 54005, doi:10.1209/0295-5075/115/54005.

Thornton, C. (2000). Numerical simulations of deviatoric shear deformation of granular media. *Géotechnique* **50**, No. 1, 43–53, doi:10.1680/geot.2000.50.1.43.

Šmilauer, V. *et al.* (2015). Reference manual. In *Yade Documentation 2nd ed*, The Yade Project, doi:10.5281/zenodo.34045, http://yade-dem.org/doc/.

Wang, J., Chi, S., Shao, X. & Zhou, X. (2021). Determination of the mechanical parameters of the microstructure of rockfill materials in triaxial compression dem simulation. *Computers and Geotechnics* **137**, 104265, doi:10.1016/j.compgeo.2021.104265.

Weiler, W. A. & Kulhawy, F. H. (1982). Factors affecting stress cell measurements in soil. *Journal of the Geotechnical Engineering Division* **108**, No. 12, 1529–1548, doi:10.1061/AJGEB6.0001393.

Wu, M., Wang, J., Russell, A. & Cheng, Z. (2021). Dem modelling of mini-triaxial test based on one-to-one mapping of sand particles. *Géotechnique* **71**, No. 8, 714–727, doi:10.1680/jgeot.19.P.212.

Xie, Y., Yang, Z., Barreto, D. & Jiang, M. (2017). The influence of particle geometry and the intermediate stress ratio on the shear behavior of granular materials. *Granular Matter* **19**, No. 2, 35, doi:10.1007/s10035-017-0723-8.

Zhou, W., Liu, J., Ma, G. & Chang, X. (2017). Three-dimensional DEM investigation of critical state and dilatancy behaviors of granular materials. *Acta Geotechnica* **12**, 527–540, doi:10.1007/s11440-017-0530-8.